

## **Electrochemical Corrosion Behavior of as-cast Zn-rich Zn-Mg Alloys in a 0.06M NaCl Solution**

*Talita A. Vida<sup>1</sup>, Emmanuelle S. Freitas<sup>1</sup>, Noé Cheung<sup>1</sup>, Amauri Garcia<sup>1</sup>, Wislei R. Osório<sup>2, 3,\*</sup>*

<sup>1</sup> Department of Manufacturing and Materials Engineering, University of Campinas, UNICAMP, 13083-860, Campinas, SP, Brazil

<sup>2</sup> School of Applied Sciences / FCA, Research Group in Manufacturing Advanced Materials, University of Campinas, UNICAMP, Limeira, SP, Brazil

<sup>3</sup> School of Technology, University of Campinas–UNICAMP, Limeira, SP 13484-332, Brazil

\*E-mail: [wislei.osorio@fca.unicamp.br](mailto:wislei.osorio@fca.unicamp.br)

*Received:* 1 March 2017 / *Accepted:* 23 April 2017 / *Published:* 12 May 2017

---

The electrochemical corrosion behavior of as-cast samples of Zn- 1.2 wt.% and Zn- 2.0 wt.% Mg alloys, solidified under similar cooling rates, is investigated in the present study. A stagnant and naturally aerated 0.06 M NaCl solution at 25 °C was used in the corrosion tests. In order to evaluate the corrosion resistance, electrochemical impedance spectroscopy (EIS) plots, potentiodynamic polarization curves and an equivalent circuit are used. It is found that the increase in the alloy Mg content (from 1.2wt.% to 2.0wt.%) refines both the Zn-rich dendritic matrix and the eutectic mixture and decreases the volume fraction of the Zn-rich phase. Consequently, this is shown to affect the cathode-to-anode area ratio, which decreases affecting the corrosion behavior. The experimental corrosion parameters demonstrated that the Mg content is associated with susceptibility to pitting corrosion.

---

**Keywords:** Zn-Mg alloys; solidification; microstructure; impedance; polarization.

### **1. INTRODUCTION**

Zn–Mg alloys are widely applied in the automotive industry and in the manufacture of portable instruments [1]. Zn has emerged as a promising bioabsorbable material, having micronutrient and supplementation properties [2-4] associated with non-toxicity and being essential in the human body. However, as-cast Zn has mechanical properties that are far too low for application as biomaterials, these properties have to be improved by the addition of alloying elements and thermomechanical treatments. Mg has been extensively studied as a biocompatible metal and hence emerges as a natural

alloying element that could be added to Zn with a view to providing superior mechanical properties [5-10]. Zn-Mg alloys also appear as a biodegradable material [11] for use in load-bearing implants [10-12] and cardiovascular stent applications [13-14].

It is well-known that a biodegradable material dissolves progressively and is absorbed in the body [15]. This characteristic constitutes a solving to restenosis, thrombosis, and irritation/inflammation reactions [8-10]. Besides, the biodegradation property is an excellent characteristic permitting a second surgery for implant removal to be unnecessary [2]. From the metallurgical point of view, regardless of the material investigated, the role of the imposed cooling rate during casting on the microstructural array and consequently on the final application properties is widely recognized [16-20]. Considering the Zn-Mg alloys, the cooling rate is also expected to have an important role on the resulting properties, *e.g.* mechanical strength and electrochemical behavior.

On one hand, it is widely known that both Mg and Mg-based alloys consist in greatly active systems, and, due to galvanic corrosion, the material is drastically and rapidly deteriorated [21-23]. On the other hand, Alves and coauthors [2] and Liu and other [24] have reported that Zn exhibits compatible physiological corrosion. However, under load-bearing condition Zn has its drawback exposed. In this sense, the addition of Mg to Zn improves both the tensile strength and elongation while preserving the biocompatibility [2]. Although some experimental studies reported that Mg reasonably improves the mechanical behavior of Zn [1-2], the literature is scarce on studies of electrochemical behavior of Zn-Mg alloys [1]. Yao and colleagues [1] have demonstrated that a nanostructured Zn- 3 wt.% Mg casting alloy has a corrosion current density of about 1/3 lower than that of a pure Zn sample. They have also reported a resulting microstructure array with the eutectic mixture containing the  $Mg_2Zn_{11}$  intermetallic compound (IMC).

Liu and Jones [25-26] investigated the microstructure evolution of Zn-Mg alloys (up to 4.5 wt.% Mg) during steady-state growth, using a Bridgman technique, in a range of growth rates from 0.001 to 8 mm/s at a temperature gradient of 15K/mm. They reported the occurrence of a dendritic primary Zn-rich phase with the eutectic phase having different morphologies, that is, rod-like, spherulitic and spiral. In a recent study of unsteady solidification of Zn-Mg alloys (0.3 to 1.2 wt.% Mg), microstructure arrays constituted by a Zn-rich matrix of different morphologies and competitive eutectic mixtures ( $Zn-Zn_{11}Mg_2$  and  $Zn-Zn_2Mg$ ) have been reported [27]. Under the high cooling rates regime, plate-like cells prevailed for dilute Zn- 0.3 wt.%- Mg and Zn- 0.5 wt.% Mg alloys, followed by a granular/dendritic transition with the decrease in cooling rate. With the increase in the alloy Mg content (1.2wt.%Mg), the Zn-rich matrix was shown to be formed only by equiaxed dendritic grains in the entire range of experimental cooling rates examined. Experimental growth laws relating the plate-like cells interphase spacing, the secondary dendritic arm spacing, and the eutectic interphase spacing with solidification thermal parameters have been proposed [27].

As pointed out by Yao and coauthors [1], detailed studies on the electrochemical behavior of Zn-Mg alloys are scarce in the literature. In this sense, this experimental investigation focus on the evaluation of the electrochemical impedance spectroscopy (EIS) and potentiodynamic polarization parameters of as-cast Zn-1.2 and 2.0 wt.% Mg alloys samples in a 0.06 M NaCl solution at the environmental temperature. The alloys samples examined had their solidification cooling rates parameterized at about 3.8°C/s, permitting only the effect of the alloy Mg content on the resulting

microstructure to be evaluated. With this, despite the similar microstructural arrangements of both alloys samples, the difference in Mg content will induce distinct eutectic fractions and dendritic and eutectic interphase spacings. This is expected to induce also distinct electrochemical corrosion behavior for each sample examined. A typical equivalent circuit (EC) containing an inductor element will also be used to evaluate the corrosion behavior.

## 2. EXPERIMENTAL

### 2.1 Alloys samples and microstructure

Commercial pure (c.p.) Mg (containing 0.11 wt.% Al, 0.01 wt.% Zn, 0.01 wt.% Mn, 0.01 wt.% Cr, and 0.01 wt.% Fe) and electrolytic Zn (containing 0.015 wt. % Fe, 0.012 wt.% Pb and 0.003 wt.% Si) were used to prepare the Zn- 1.2 wt.% and 2.0 wt.% Mg alloys. The samples were extracted from specific positions along the length of directionally solidified castings of both alloys, having a similar solidification cooling rate of about 3.8 °C/s. For this, a water-cooled directional solidification setup was used, as detailed in a previous study [27]. To determine the cooling rates during solidification, eight type K thermocouples were placed in the geometrical center of the mold cavity along the length of the castings, with the temperature data acquired automatically and stored in a computer.

A Nital 10 % etchant (ethanol and nitric acid solution) applied during 7 seconds was used to reveal the microstructure, which was analyzed by an Olympus Inverted Metallurgical Microscope (model 41GX). From the optical images of the samples, both the eutectic ( $\lambda_{\text{eut}}$ ) and secondary dendritic arm ( $\lambda_2$ ) spacings were analyzed and measured. The average values of these aforementioned microstructure parameters were taken from about 40 measurements on longitudinal sections of each alloy sample. To complement the microstructural characterization, a ZEISS® SEM/scanning electron microscope (ZEISS®, model EVO-MA15) with EDS (energy dispersive spectroscope) probe (OXFORD-X-MAX) was also used. In order to carry out the analyses of the phases forming the microstructure of the Zn-Mg alloys, an X-ray diffraction technique using a PANalytical X'Pert, model Pro MRD was used. The patterns were obtained by the XRD diffractometer with a 2-theta range from 20 to 95 degrees and Cu-K $\alpha$  radiation with a wavelength of 0.15406 nm.

### 2.2 EIS and potentiodynamic evaluations

A conventional three-electrode system, containing an Ag/AgCl reference electrode, a platinum wire as a counter electrode (area higher than the sample area) and the Zn-Mg alloy samples as the working electrodes, were used. Before all corrosion tests, *i.e.* EIS (electrochemical impedance spectroscopy) and potentiodynamic polarization, the Zn-1.2 and 2.0 wt.% Mg alloys samples were carefully ground using a 1200 grit SiC paper and polished using 1  $\mu\text{m}$  diamond paste. A naturally aerated and stagnant 0.06 M NaCl solution was used as the electrolyte at an environmental temperature of 25 ( $\pm$  2) °C. A potentiostat/galvanostat Autolab® model PGSTAT-128N was used. The linear polarization tests were performed using the aforementioned electrochemical cell kit, NaCl solution

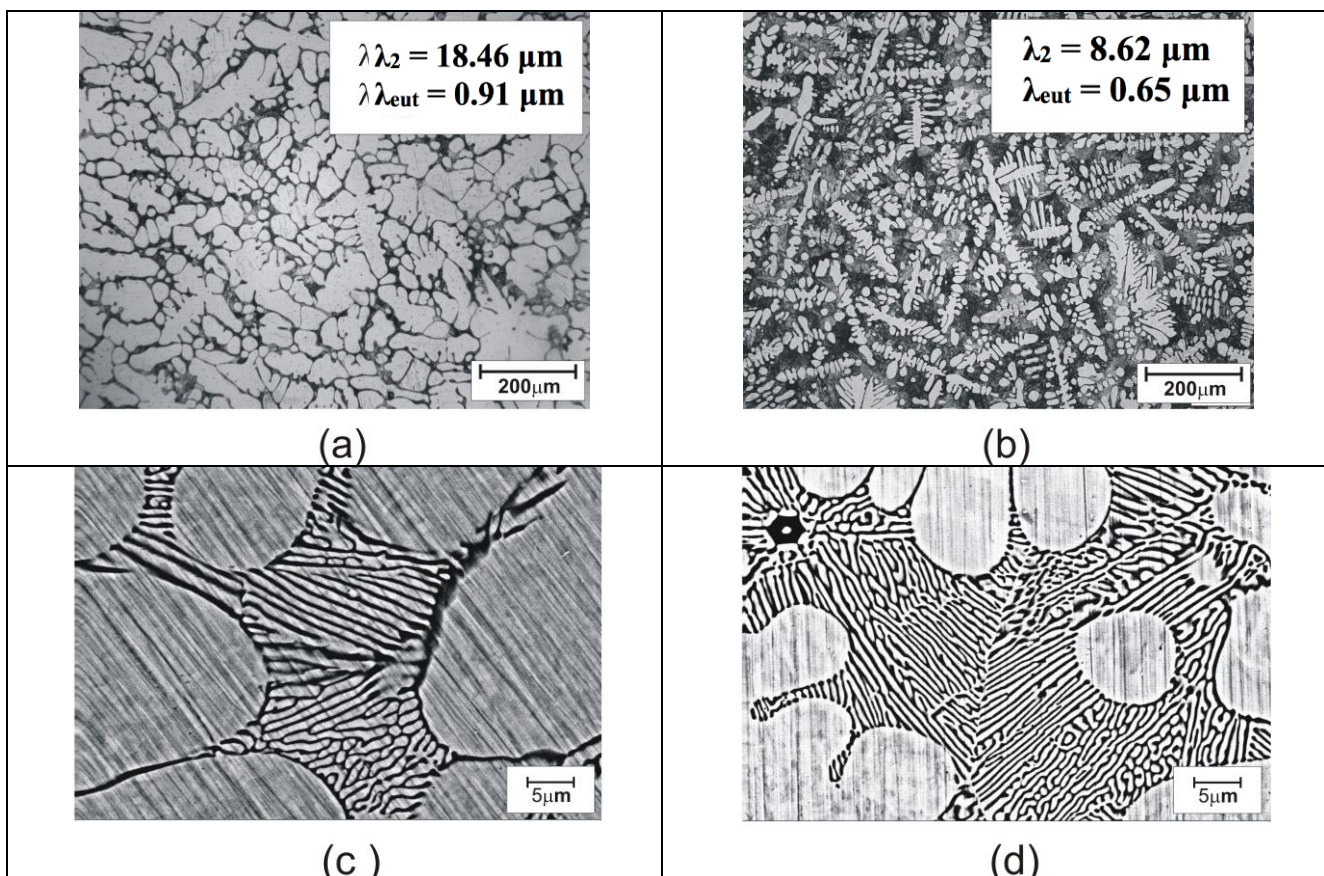
with the Zn-Mg alloy samples having surface areas of about 0.5 cm<sup>2</sup> totally immersed. Triplicate tests were carried out with each alloy sample.

With a view to attaining steady state conditions, the EIS measurements have been initiated after 20 minutes of immersion of each Zn-Mg alloy sample into the mentioned electrolyte. Additionally, OCP (open-circuit potential) was adopted during about 15 minutes to ensure reasonable steady state conditions. EIS tests were carried out using a potential amplitude adjusted at 10 mV (SCE), peak-to-peak (AC signal) at open-circuit. In the frequency range between 10<sup>5</sup> Hz to 10<sup>-2</sup> Hz, ten points per decade were selected. For quantification of the experimental EIS parameters, an equivalent circuit (EC) was adopted, using the ZView<sup>®</sup> software, version 2.1b. A conventional and typical EC describing two CPEs (constant-phase element) and two resistors with an inductor element was used. CNLS (complex non-linear least squares) simulations and experimental data were compared and chi-square ( $\chi^2$ ) values and the sum of squares have been determined.

Polarization tests were carried out immediately after each EIS test. These polarization tests were conducted at a scan rate of 0.167 mV/s from -1100 mV to -700 mV (Ag/AgCl) vs. OCP. The current densities ( $i_{corr}$ ) were estimated from the potentiodynamic polarization curves, by Tafel's extrapolation, taking into account preferentially the cathodic branch.

### 3. RESULTS AND DISCUSSION

#### 3.1. Microstructural characterization



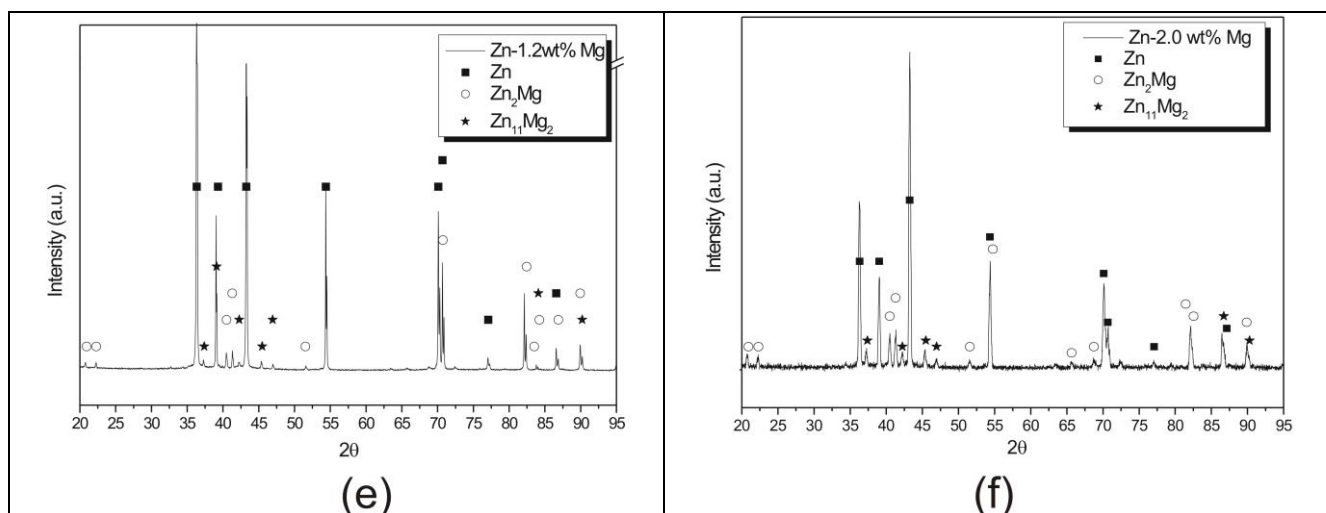


**Figure 1.** Microstructural arrays of: (a) and (c) Zn-1.2 wt.% Mg; (b) and (d) Zn- 2.0 wt.% Mg as-cast alloys; and (e) and (f) their corresponding XRD patterns, respectively.

Fig. 1 shows typical as-solidified microstructures of Zn-1.2 and 2.0 wt.% Mg alloys. It is worth noting that these two distinct Zn-Mg alloys samples were extracted from directionally solidified castings, as aforementioned. Although having different Mg contents, *i.e.* 1.2 and 2.0 wt.%, these samples were selected from specific distances along the length of each casting (30 and 20 mm from the bottom of each particular casting, respectively [27]) having very similar solidification cooling rates of about 3.8 °C/s. A Zn-rich matrix of equiaxed dendritic morphology associated with a eutectic phase (lamellar morphology) in the interdendritic regions, constitute the alloys microstructures, as shown in Figs. 1(a) and (b) for the Zn-1.2 and 2.0 wt.% Mg alloys, respectively. The eutectic mixture of both Zn-1.2 and 2.0 wt.% Mg alloys samples is highlighted in Figs. 1(c) and (d), respectively.

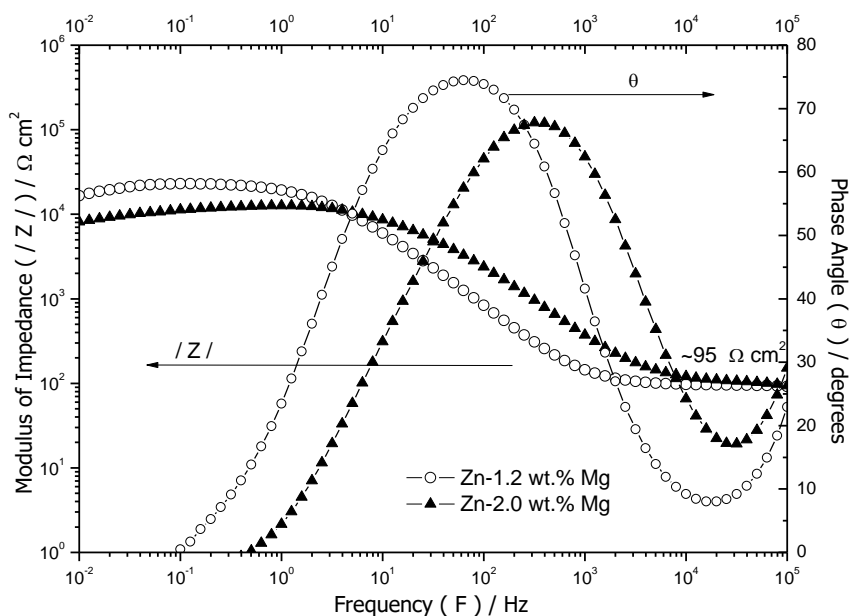
Figs. 1(e) and (f), show the experimental XRD patterns of the Zn-1.2 and 2.0 wt.% Mg alloys samples, respectively. It can be seen that the Zn-rich matrix (dendritic matrix) is predominantly constituted by a Zn-rich phase, while the  $Zn_{11}Mg_2$  and  $Zn_2Mg$  intermetallic compounds (IMCs) are associated with the eutectic mixture. These IMCs are described by the phase diagram of binary Zn-Mg alloys, and are reported to occur in a competitive way in the eutectic mixture [27]. Since the aim of this study is to evaluate the electrochemical behavior of these Zn-Mg alloys, the  $Zn_{11}Mg_2$  and  $Zn_2Mg$  IMCs have to be analyzed in terms of their potential to constitute galvanic couples with the Zn-rich matrix. In this sense, their morphologies, sizes and distribution in the microstructure, can have an important role on the corrosion resistance. Despite the similar microstructural arrays observed in Fig. 1 for both alloys samples (morphology and IMC formation), it can be seen that the scale of the microstructural parameters, *e.g.* secondary dendritic spacings ( $\lambda_2$ ) and interlamellar spacings ( $\lambda_{eut}$ ), are quite different. It is known that these parameters increase along the length of the directionally solidified casting from the cooled bottom, which is intimately associated with the progressive decrease in solidification cooling and growth rates. These  $\lambda_2$  and  $\lambda_{eut}$  are commonly described as a function of these solidification thermal parameters; cooling ( $dT/dt$ ) and growth rate in the form of power functions having  $-1/3$  and  $-2/3$  exponents, respectively [27]. For instance, an experimental growth law given by  $\lambda_2 = 28.5 (dT/dt)^{-1/3}$  for the Zn-1.2 wt.% Mg alloy has been proposed [27]. The experimental evolution

of  $\lambda_{eut}$  with both cooling rate and growth rate can also be experimentally derived, as shown in a previous study [27]. In the present study the cooling rate of the two samples examined have been parameterized at about 3.8 °C/s, and differences in  $\lambda_2$  and  $\lambda_{eut}$  are associated with the Mg content (1.2 and 2.0 wt.%).

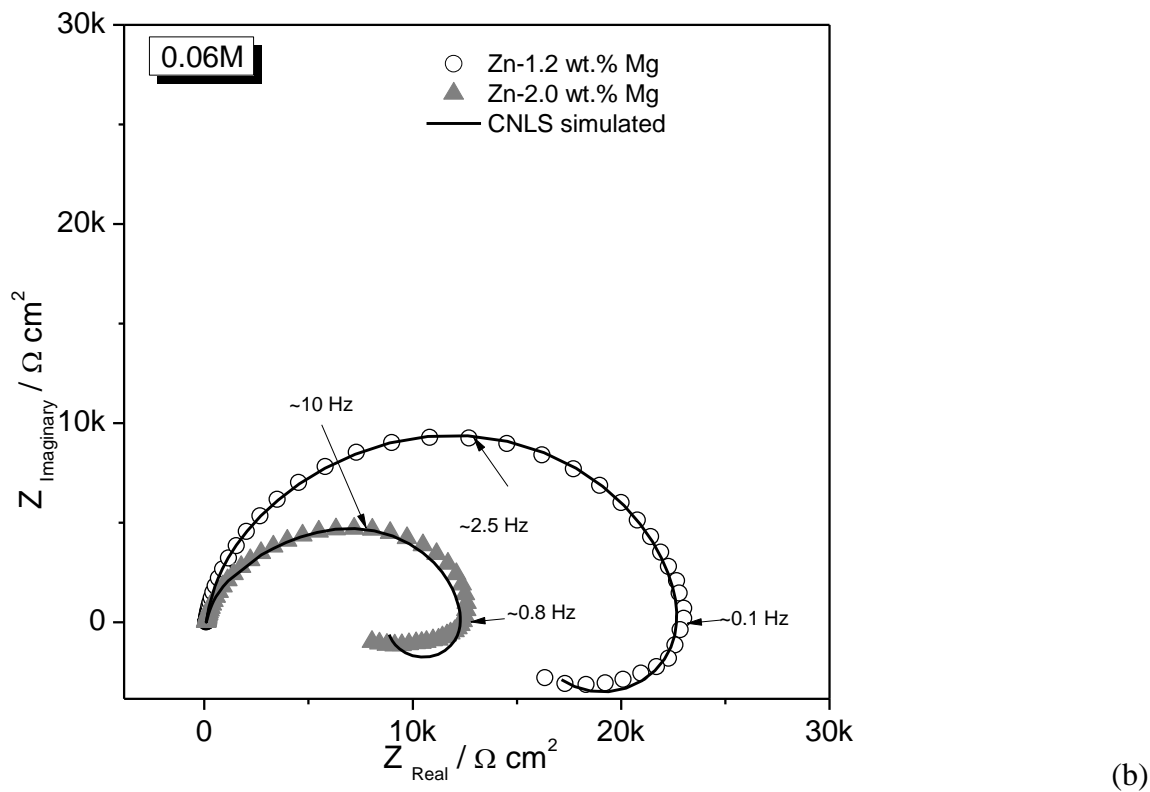
Fig. 1(a) and (b) evidences that the experimental values of  $\lambda_2$  and  $\lambda_{eut}$  are 18.46 and 0.91  $\mu\text{m}$  and 8.62 and 0.65  $\mu\text{m}$  for the Zn-1.2 wt.% Mg and Zn- 2.0 wt.% Mg alloys, respectively. It can be seen that the increase in the Mg content (from 1.2 and 2.0 wt.%) has induced a microstructural refinement, *i.e.*  $\lambda_2$  and  $\lambda_{eut}$  decreased by a factor of 2 and 1.5 times, respectively. This was expected since Mg is known to provide a refinement effect [27]. With the increase in the alloy Mg content, the eutectic volume fraction also increases, and hence the corresponding fractions of both  $\text{Zn}_{11}\text{Mg}_2$  and  $\text{Zn}_2\text{Mg}$  IMCs also increase. That is, despite the relatively small increase in the Mg content (from 1.2 and 2.0 wt.%), the corresponding increase in the eutectic fraction and decrease in  $\lambda_2$  and  $\lambda_{eut}$ , distinct electrochemical corrosion behavior can be expected during corrosion tests of the two alloy samples.

### 3.2. EIS plots analyses

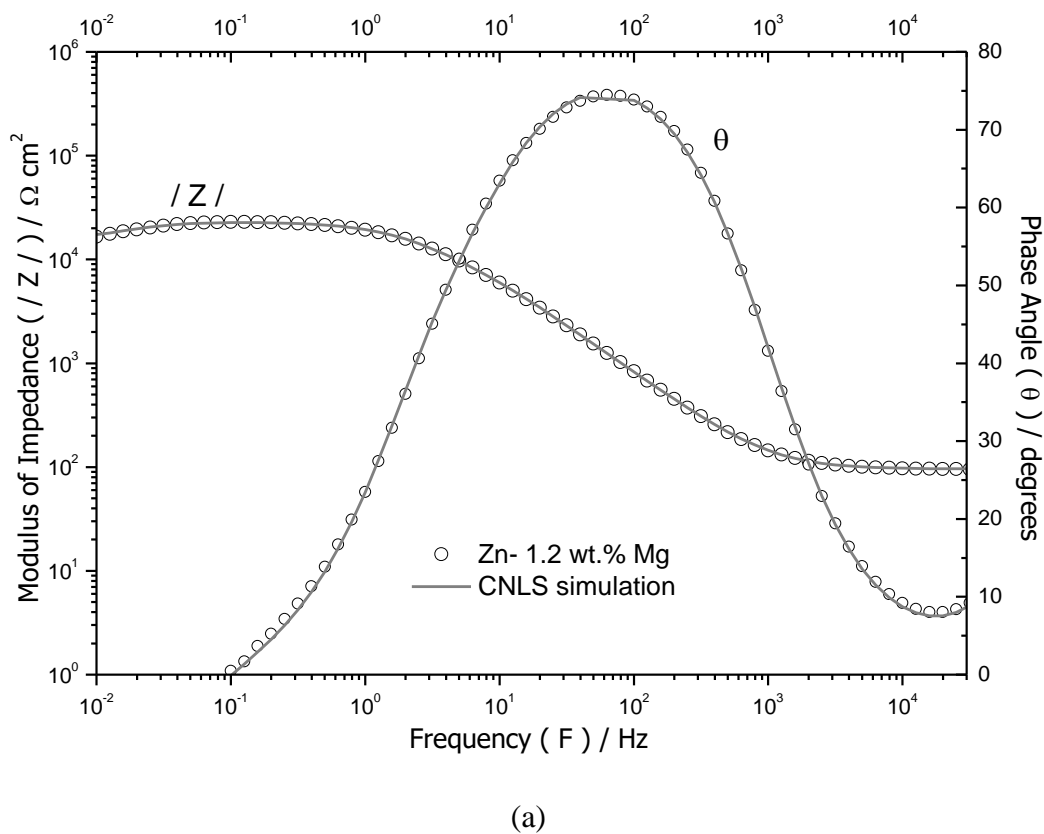
Experimental EIS plots, for the two distinct Zn-Mg alloys samples in a naturally and stagnant 0.06 M NaCl solution at room temperature (25 °C), are shown in Fig. 2. Bode and Bode-phase representations are shown in Fig. 2(a), while Nyquist plots (experimental and CNLS simulations) are shown in Fig. 2(b). Since triplicate experiments have been carried out for each alloy sample, the EIS plots in Fig. 2 represent the average values. Based on the EIS plots, mainly considering Nyquist and Bode plots, it seems that only time constants are predominant. A capacitive semi loop, from high to medium frequency ranges, and a clear inductive loop at low frequency regions are characterized. Fig. 3(a) and (b) shows both Bode and Bode-phase representation with CNLS simulations performed with the ZView® software. Discrepancies between the experimental data and CNLS simulations are more visible in Nyquist plots, as shown in Fig. 2(b).



(a)



**Figure 2.** Comparison of experimental results for: (a) Bode and Bode-phase plots and (b) Nyquist plots with CNLS simulated and experimental results in a 0.06 M NaCl solution at 25°C for Zn-1.2 and 2.0 wt.% Mg alloys.



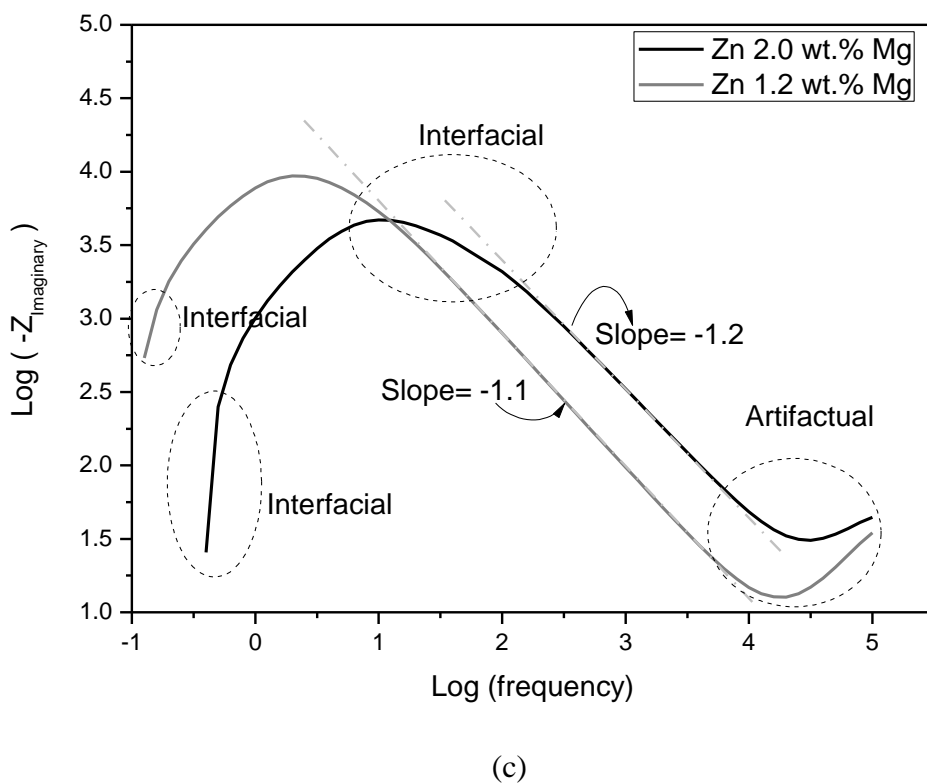
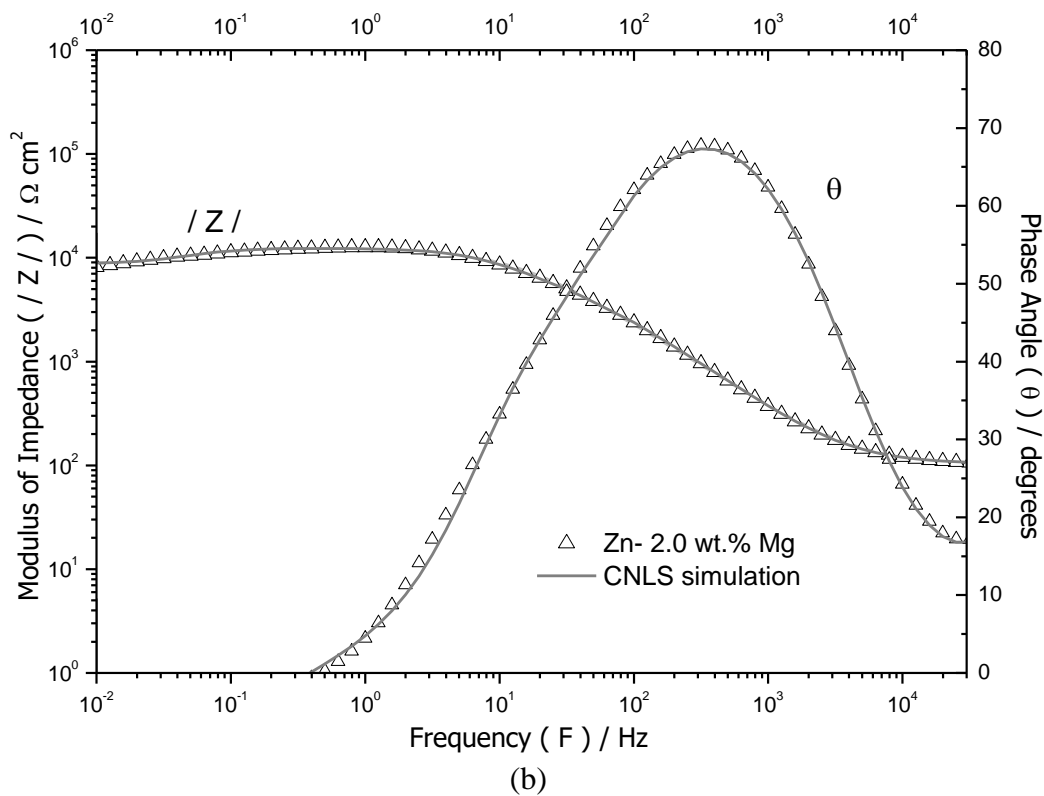


**Figure 3.** Experimental and CNLS simulations in Bode and Bode-phase representations for (a) Zn-1.2 wt.% Mg and (b) Zn- 2.0 wt.% Mg alloys; and (c) the moduli of the imaginary parts of the impedances vs. frequencies of the two alloys examined.

In order to understand if two or three time constants describe the electrochemical corrosion behavior of the Zn-Mg alloys samples examined, the Bryan Hirschorn and collaborators method has been used [28-30], as shown in Fig. 3(c), in which the moduli of the imaginary parts of the impedances vs. frequencies of the two alloy samples examined are plotted. Slopes of -1.1 and -1.2 for Zn-1.2 wt.% Mg and Zn-2.0 wt.% Mg alloy samples have been determined. Based on this method, the occurrence of two time constants is suggested. Between  $10^4$  Hz and  $10^5$  Hz, it seems that a time constant is intimately associated with artefactual effects and not interfacial ones. So, when the CNLS analysis is carried out, the experimental point between  $10^4$  Hz and  $10^5$  Hz has not been considered. This will be discussed in detail in the next section.

Because two constant times are occurring, a capacitive semi loop in high frequency ranges constituting the first time constant is characterized. This capacitive behavior seems to be associated with charge transfer reactions between the surfaces of the alloys samples and the electrolyte, thus permitting a double layer to be formed. The second time constant initiates in a range of frequencies from about 1 Hz toward lowest frequencies and an inductor element is established. Associated with this second time constant, it seems that mass transport associated with diffusion/adsorption of ions and intermediates throughout the corrosion product layer due to pitting formation is favored, as reported by Jamesh and coauthors [10].

Three time constants were recently considered by Alves and collaborators [2] in order to describe the electrochemical behavior of electrodeposited (coated) Zn-1, 2 and 3 wt.% Mg alloys. Based on both Bode and Bode-phase shaped plots, two time constants are reasonably characterized. However, due to the high frequency range, all the three Zn-Mg alloys examined have not shown plateaus of moduli of impedance ( $|Z|$ ) associated with corresponding phase angles approaching  $30^\circ$ , but rather they approached  $0^\circ$  [1; 31]. Since the plateau has phase angle close to zero, no reaction forming oxide films (or corrosion by-product) can be characterized. Consequently, only two time constants are exhibited by the alloy corrosion system.

Comparisons between Bode and Bode-phase diagrams of two alloys samples, between  $10^{-2}$  Hz and  $10^0$  Hz, evidence that  $|Z|$  with frequency favors the Zn-1.2 wt.% Mg alloy with their corresponding  $|Z| = \sim 17 \text{ k}\Omega \text{ cm}^2$  and  $|Z| = \sim 8 \text{ k}\Omega \text{ cm}^2$ , respectively. Similar sequence is also observed when Bode-phase plots are also analyzed. The Zn- 1.2 wt.% Mg alloy sample has a maximum phase angle ( $\theta$ ) of  $\sim 74^\circ$  at 64 Hz, while the Zn- 2.0 wt.% Mg alloy has a maximum  $\theta$  of  $\sim 68^\circ$  in a frequency of about 5 x higher than that of the Zn-1.2 wt.% Mg alloy. From these comparative and qualitative observations, a better electrochemical corrosion resistance is associated with the Zn-1.2 wt% Mg alloy sample. This seems to be intimately associated with the fact that the lower Mg content (active material) also induces a lower eutectic fraction (ef) and, consequently, the cathode-to-anode area ratio also decreases. This is directly associated with the formation of galvanic couples between the Zn-rich phase (dendritic matrix) and the IMCs of the eutectic region located in the interdendritic areas, as shown in Fig. 1.

Another analysis that can also be made concerning the Bode plot between  $10^3$  and  $10^0$  Hz, indicated a linear slope of about -1 for the two alloys samples examined. A capacitive behavior associated with the nature of the double electronic layer formation is indicated. Based on the Bode diagrams, similar double layers are formed for the two samples examined.

Finally, between  $10^4$  and  $10^5$  Hz, the Bode diagram indicates that the electrolyte resistance dominates the impedance. Additionally, the Bode-phase plots at the same frequency range (*i.e.* between  $10^4$  and  $10^5$  Hz) should indicate a phase angle close to zero. Since the surfaces of all samples examined were carefully prepared and immersed in similar conditions in the electrolyte, and the experimental results indicate phase angle close to  $30^\circ$  at  $10^5$  Hz, it seems that an artefactual effect occurred and hence the corresponding experimental point has not been considered.

A qualitative analysis of Nyquist plots (Fig. 2b) permits also to infer that the Zn-1.2 wt.% Mg alloy sample demonstrates a nobler character when compared with that of the Zn- 2.0 wt.% Mg alloy. In order to provide a more consistent discussion, and permitting the impedance parameters to be quantified, a typical EC is proposed and discussed.

### 3.3. Equivalent circuit (EC) analysis

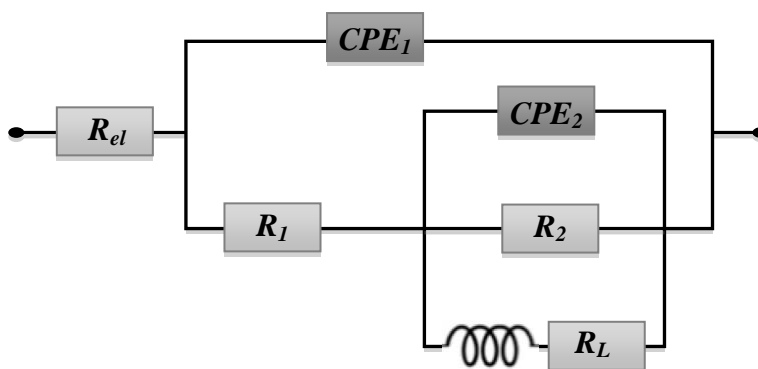
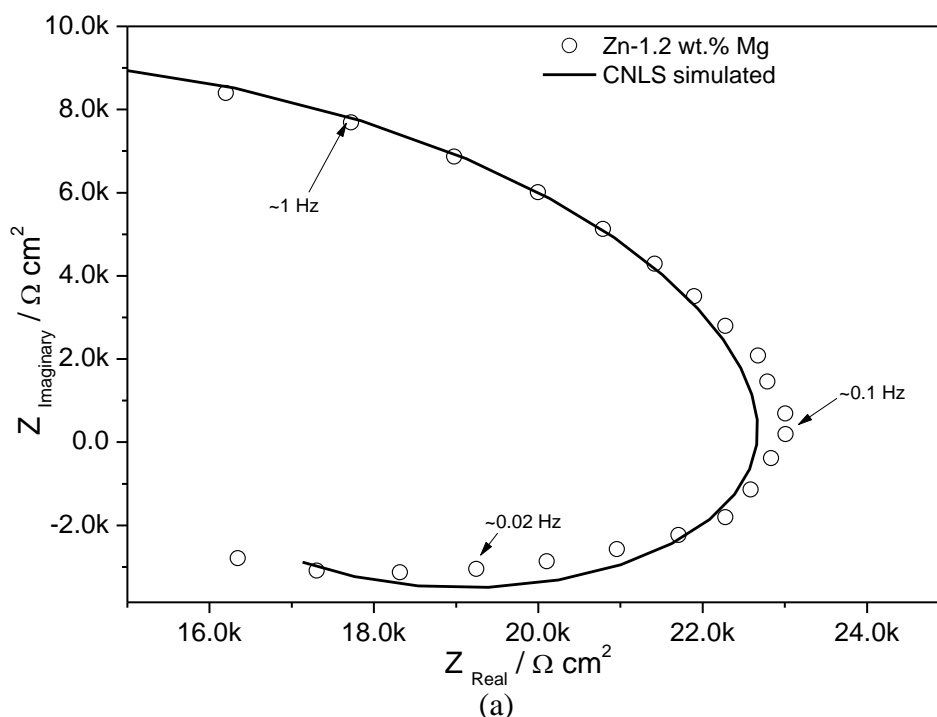
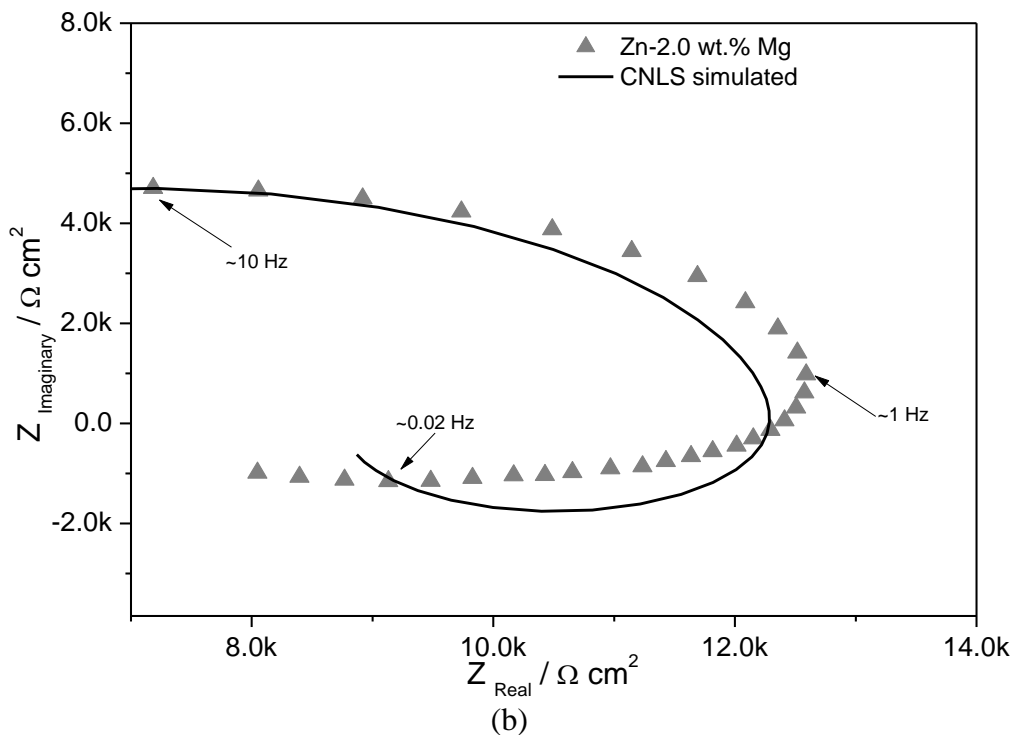


Figure 4. Proposed equivalent circuit (EC).





**Figure 5.** Partial Nyquist plots at low frequency ranges for: (a) Zn-1.2 wt.% Mg and (b) Zn- 2.0 wt.% Mg alloys.

**Table 1.** Impedance parameters of the two Zn- 1.2 wt.% and 2.0 wt.% Mg alloys examined in a 0.06M NaCl solution

Parameters	Zn-1.2Mg	Zn-2.0Mg
$R_{el} (\Omega \text{ cm}^2)$	95 ( $\pm 0.2$ )	95 ( $\pm 0.2$ )
$CPE_{(1)} (10^{-6} \text{ Fcm}^2)$	3.0 ( $\pm 0.03$ )	0.41 ( $\pm 0.01$ )
$R_1 (\Omega \text{ cm}^2)$	89 ( $\pm 70$ )	90 ( $\pm 75$ )
$n_1$	0.93	0.96
$CPE_{(2)} (10^{-6} \text{ Fcm}^2)$	2.7 ( $\pm 0.3$ )	2.1 ( $\pm 0.1$ )
$R_2 (10^3 \Omega \text{ cm}^2)$	23.9 ( $\pm 0.2$ )	12.5 ( $\pm 0.1$ )
$n_2$	0.49 ( $\pm 0.02$ )	0.73
$L (10^3 \text{ Hcm}^2)$	477 ( $\pm 22$ )	99 ( $\pm 8$ )
$R_L (10^3 \Omega \text{ cm}^2)$	46.2 ( $\pm 1.7$ )	28.1 ( $\pm 1.5$ )
$\chi^2$	13 $10^{-4}$	63 $10^{-4}$
Sum of Sqr.	0.16	0.74

In order to evaluate the experimental and CNLS simulations, thus permitting impedance parameters to be obtained, an EC with inductor has been adopted (Fig. 4). This kind of EC has been widely used in recent studies for a number of distinct materials and alloys [10, 32-35]. Experimental and CNLS simulated results in Nyquist representation are shown in Fig. 2(b).

Comparison between experimental and CNLS simulated result, in Bode and Bode-phase plots, are also shown Fig. 3(a) and (b). Partial Nyquist plots at low frequency ranges are shown in Fig. 5(a) and (b). The quality of the experimental/simulated fit has been characterized by chi-square ( $\chi^2$ ) values. The sums of squares (provided by the ZView<sup>®</sup> software) for each sample examined are also shown in Table 1.

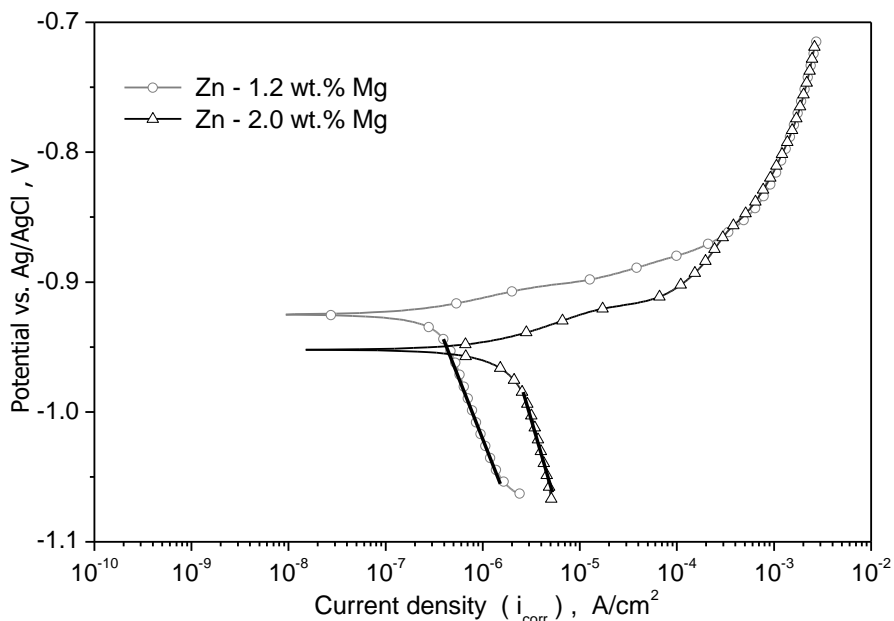
Considering the proposed EC,  $R_{el}$  is the resistance of the electrolytic solution, *i.e.* about  $95 \Omega\text{cm}^2$ . At high frequency limit ( $F > 10^4$  Hz) in a Bode plot (shown in Fig. 3(a) and (b)), the electrolyte resistance is easily detected.  $R_1$  and  $R_2$  correspond to the resistances for charge transfer of the porous (outer) layer and barrier (inner) layer, respectively. These parameters are intimately associated with the dissolution of the alloy sample (metallic corrosion) and the corrosion product (*e.g.* hydrous oxides formation into the pores of this layer) and the charge transfer resistance (anodic behavior) through the outer (porous) layer and the participation of adsorbed intermediates (inner layer), respectively. The capacitances, associated with the porous corrosion product layer and that with the double layer, are represented by  $CPE_{(1)}$  and  $CPE_{(2)}$ , respectively. An inductor element and its corresponding resistance are also considered. Inductive loops are attributed to the adsorption and falling of the corrosion products at the interface between the electrolyte and the sample [33; 35]. Mg-rich Zn alloys were considered in these two aforementioned studies [10; 33]. Relaxation of species in the oxide layer due to adsorption and incorporation of Cl ions into the oxide film is also often considered [36-38]. The inductive loop has also been associated with pitting [39-40]. In this study, it seems that pitting causes IMCs dissolution, which potentially can also be incorporated into the corrosion by-product.

Considering the physical interpretation of the circuit elements, CPE characterizes the impedance of a phase element, and is calculated as  $CPE = [C(j \omega)^n]^{-1}$ , where C is the capacitance; j is the current (imaginary number:  $-1^{0.5}$ );  $\omega$  is the angular frequency and  $-1 \leq n \leq 1$  [10, 33-40]. When CPE has  $n = 1$ , an ideal capacitor is defined. A distribution of relaxation times in the frequency space is represented when  $0.5 < n < 1$  [33-40].

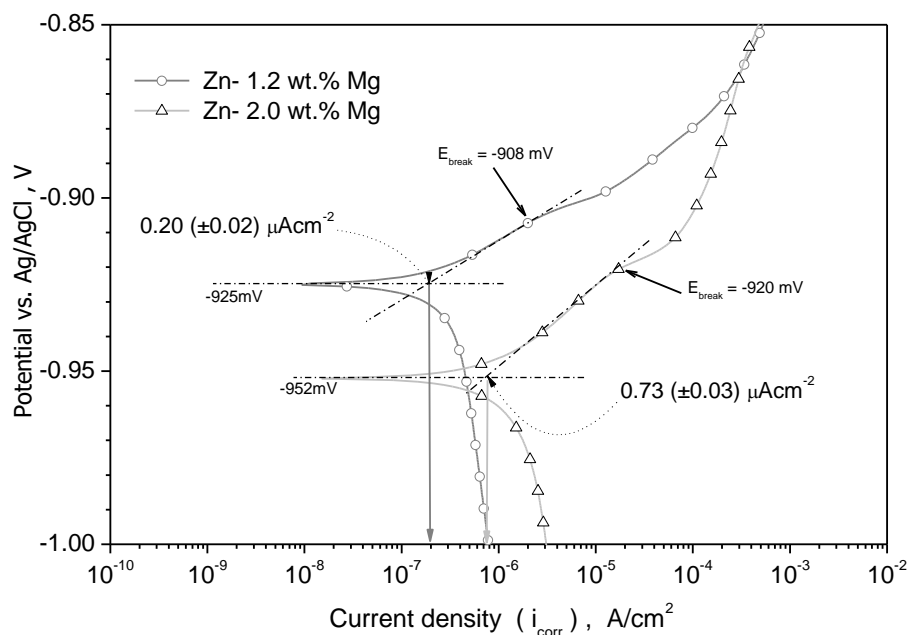
By analyzing the impedance parameters, shown in Table 1, it can be seen that with the increase in Mg content, *i.e.* from 1.2 wt.% to 2.0 wt.%, the corrosion resistance decreased. It is clearly observed that the porous resistances ( $R_1$ ) are considerably lower than those of the inner oxide layers resistances  $R_2$ . Both Zn-1.2 and 2.0 wt.% Mg alloys samples have similar  $R_1$ , which indicates a similar initial corrosion mechanism associated with the double layer formation up to the initial porous oxide layer formation. On the other hand, when  $CPE_{(2)}$  and  $R_2$  are analyzed, it is clearly observed that  $CPE_{(2)}$  are of the same order of magnitude, while  $R_2$  unequivocally indicates higher corrosion resistance associated with the Zn- 1.2 wt.% Mg alloy sample. However, the “n” parameter indicates the occurrence of pitting. When the inductor parameters are analyzed, the inductance “L” and resistance “ $R_L$ ” is about 5 and 1.6 times higher, respectively, for the Zn- 1.2 wt.% Mg alloy when compared with the corresponding values of the Zn- 2.0 wt.% Mg alloy. This indicates that pitting seems to be more drastic and deeper with the increase in the alloy Mg content.

3.4 Potentiodynamic polarization

Since EIS parameters have indicated that the Zn- 1.2 wt.% Mg alloy has a better electrochemical behavior than that of the Zn- 2.0 wt.% Mg alloy, potentiodynamic polarization curves were also analyzed. It is worth noting that all polarization tests were conducted immediately after each EIS test.



(a)



(b)

**Figure 6.** Experimental potentiodynamic polarization curves: (a) anodic and cathodic branches between -1.1 V and -0.7 V (vs. Ag/AgCl) and (b) between -1.0 V and -0.85V (vs. Ag/AgCl) for the Zn-1.2 wt.% Mg and Zn- 2.0 wt.% Mg alloys.

Fig. 6 shows typical experimental potentiodynamic polarization curves for both the Zn- 1.2 wt.% Mg and Zn- 2.0 wt.% Mg alloys samples. Complete anodic and cathodic branches between -1.1 V and -0.7 V (vs. Ag/AgCl) can be seen in Fig. 6(a). In order to determine the experimental current density ( $i_{\text{corr}}$ ) the potential range between -1.0 V and -0.85V (vs. Ag/AgCl) was considered. Tafel's extrapolation was used to determine the  $i_{\text{corr}}$  values, taking into account preferentially the cathodic branch, as shown in Fig. 6(b). In a general analysis, it can be concluded that the increase in the alloy Mg content has displaced the potential toward a more active side (about 27 mV toward the more active potential), associated with increase in  $i_{\text{corr}}$  (of about 3.5 times), as shown in Fig. 6(b). Besides, it can also be seen that the potential break ( $E_{\text{break}}$ ) also indicates nobler behavior of the Zn- 1.2 wt.% Mg alloy sample. When  $E_{\text{break}}$  is displaced toward a more active potential, this is associated with more susceptibility to pitting. The aforementioned results are in agreement with the EIS parameters, mainly when both  $L$  and  $R_L$  are considered, since higher  $R_L$  indicates lower susceptibility to pitting.

Considering the experimental results of  $i_{\text{corr}}$ , corrosion potential and break potential for the two Zn-Mg alloy samples examined, it can be seen that the Zn- 1.2 wt.% Mg alloy sample has  $i_{\text{corr}}$  of about  $0.20 \pm 0.02 \mu\text{A cm}^{-2}$  associated with a corrosion potential  $E_{\text{corr}} = -925\text{mV}$  (vs. Ag/AgCl) and  $E_{\text{break}} = -908\text{mV}$  (vs. Ag/AgCl). After  $E_{\text{corr}}$  is attained, a slight and partial stabilization on current density from  $0.4 \times 10^{-6} \text{ A cm}^{-2}$  (~918 mV) up to  $2.1 \times 10^{-6} \text{ A cm}^{-2}$  (~908 mV) for the Zn- 1.2 wt.% Mg can be observed. Sequentially, after -908 mV (vs. Ag/AgCl) the anodic current density increases rapidly, as indicated by the arrows in Fig. 6(b). This is directly associated with the breakdown potential ( $E_{\text{break}}$ ), which means physically that some oxide film or corrosion by-product or intermediate species (partially passive) is partially broken, thus permitting, for instance, that chloride ions penetrate throughout the oxide film and the microstructure of the alloy examined is reached. This phenomenon also occurs with the Zn-2.0 wt.% Mg alloy, but at a slightly more active potential. For example, the difference between  $E_{\text{break}}$  and  $E_{\text{corr}}$  for the Zn-2.0 wt.% Mg alloy is approximately 2 times higher than that observed for the Zn-1.2 wt.% Mg alloy, *i.e.* 32 mV against 17 mV, respectively.

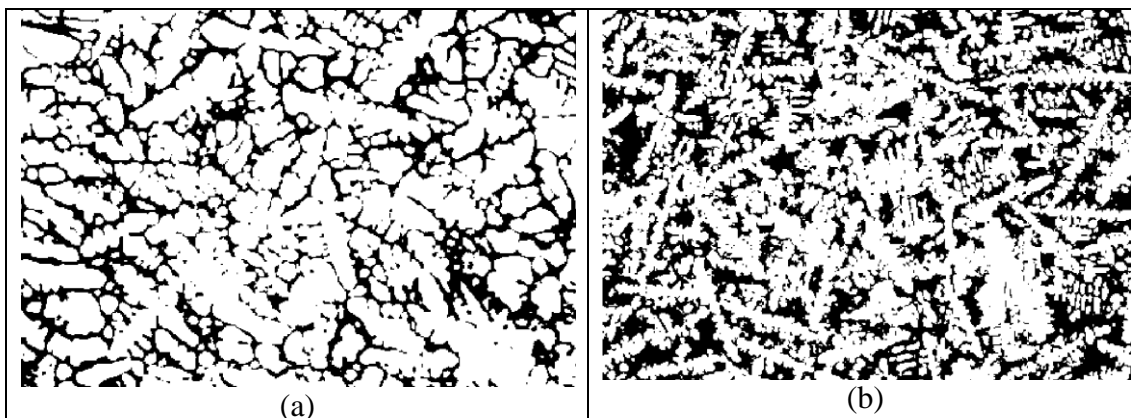
Another interesting observation, provided from the experimental potentiodynamic polarization curves, is concerned to the plateaus of cathodic current density, as shown in Fig. 6(a). These plateaus occur between about -1060 mV and -943 mV and between -1060 and -988mV (Ag/AgCl) for the Zn-1.2 wt.% Mg and Zn-2.0 wt.% alloys, respectively. These observed ranges of plateaus can be associated with a limiting cathodic current density for dissolved gases (oxygen and/or hydrogen) reduction reaction [41-43]. It has also been reported that hydrogen evolution is the predominant cathodic reaction in magnesium and magnesium alloys [44-46]. It has also been reported that magnesium in an aqueous environment will produce a partially protective surface film composed of both MgO and Mg(OH)<sub>2</sub> [44-46].

However, in the present study, Zn-rich alloys containing Mg content were examined. From the electrochemical point of view, Zn oxides at -1249mV (SCE) [47] reacting as  $\text{Zn} + 2\text{OH}^- \rightarrow \text{Zn(OH)}_2$ . On the other hand, Mg initially oxides at a more active potential (~ -2370 mV, SCE) or -2690 when  $\text{Mg} + 2\text{OH}^- \rightarrow \text{Mg(OH)}_2$  [47]. This suggests that the cathodic activity of the alloy sample containing more Mg has been displaced toward more active potentials and this seems to occur first, under similar conditions, for the Zn-2.0 wt.% Mg alloy sample when compared with the Zn-1.2 wt.% Mg alloy sample.

Krieg and collaborators [48] have reported that the alloy Mg content is not the main key to the enhancement of corrosion behavior of Zn-Mg alloys in the range from 1 to 3 wt.% Mg. They concluded that finer microstructures provide better corrosion resistance. Because microstructural features have important roles on the corrosion behavior, some discussions interrelating fraction of eutectic mixture, anode-to-cathode area ratio and the resulting EIS and  $i_{\text{corr}}$  results, will be conducted in next section.

### 3.5. Microstructure and corrosion behavior

From the electrochemical point of view, regardless of the phases detected, at least a galvanic couple is constituted, i.e. between the Zn-rich dendritic matrix and the eutectic mixture. Krieg and coauthors [48] have reported that  $\text{MgZn}_2$  is an IMC containing 16 wt.% of Mg. This can also be observed in the Zn-Mg phase diagram. Considering that both  $\text{Mg}_2\text{Zn}_{11}$  (or  $\text{Zn}_{11}\text{Mg}_2$ ) and  $\text{MgZn}_2$  (or  $\text{Zn}_2\text{Mg}$ ) IMCs have been detected in the Zn-1.2 wt.% and 2.0 wt.% Mg alloys, and associated with the fact that these IMCs are intrinsically located in the eutectic mixture, galvanic couples are unquestionably formed. Krieg and coauthors [48] stated that -770 mV (SHE) and -782 mV (SHE) are the corresponding potentials for Zn and  $\text{MgZn}_2$ , respectively. This evidences that the Zn-rich dendritic phase has a nobler potential with respect to Mg in the NaCl solution examined. These authors have also reported that with the increase in Mg content, the Zn-rich areas decreased and the morphology of eutectic mixture became increasingly finer [48]. This is also clearly evidenced when Fig. 1 is observed. The microstructural parameters  $\lambda_2$  and  $\lambda_{\text{eut}}$  were previously discussed and it can be seen in Fig. 1 that with the increase in the alloy Mg content, these parameters have been refined. Although XRD patterns shown in Fig. 1(e) and (f) have demonstrated that both  $\text{Zn}_{11}\text{Mg}_2$  and  $\text{Zn}_2\text{Mg}$  IMC are formed, their corresponding fractions were not determined. Actually, the eutectic mixture is constituted by both  $\text{Zn}_{11}\text{Mg}_2$  and  $\text{Zn}_2\text{Mg}$  IMCs, which associated with the Zn-rich dendritic matrix, give rise to galvanic couples.



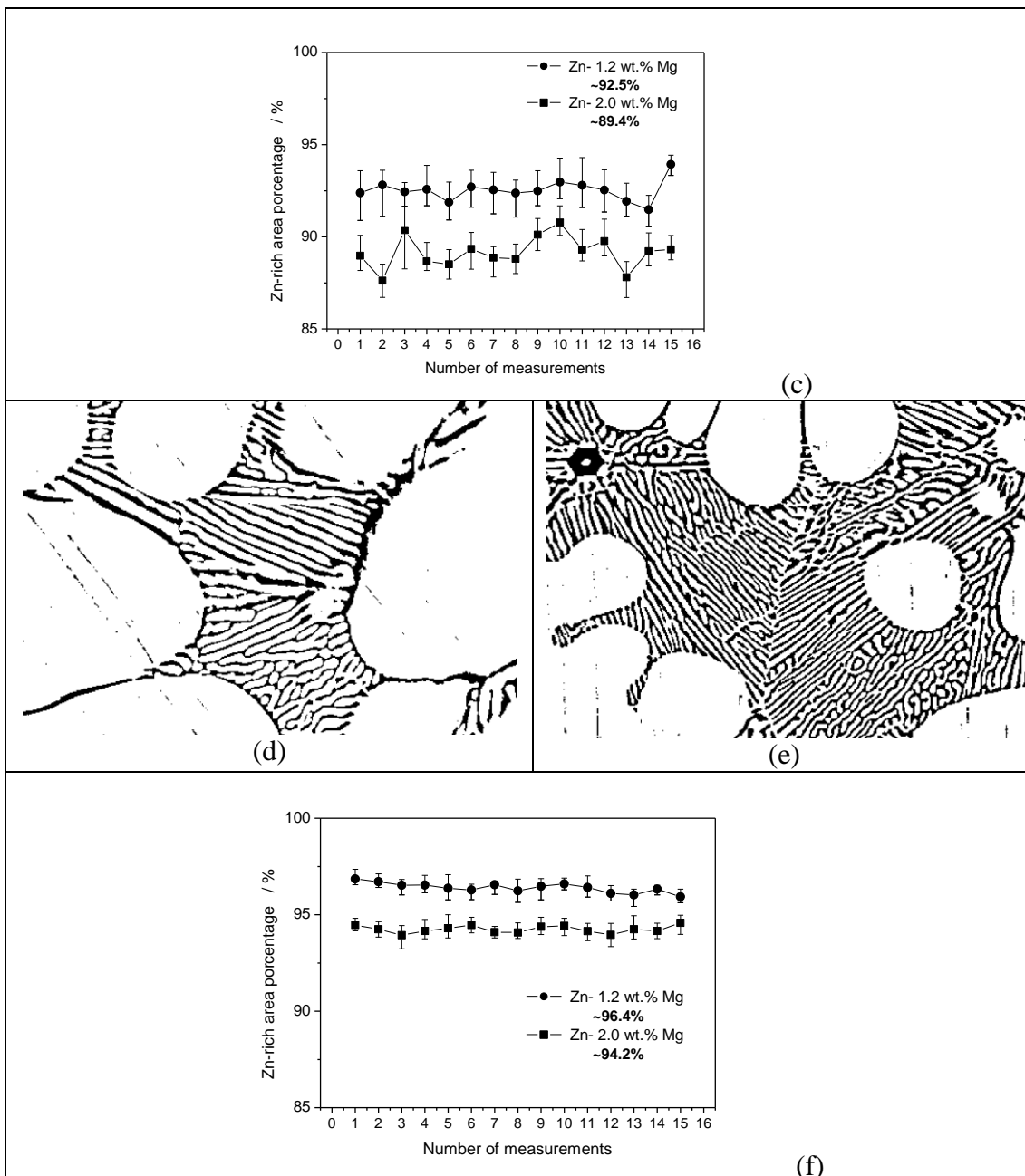


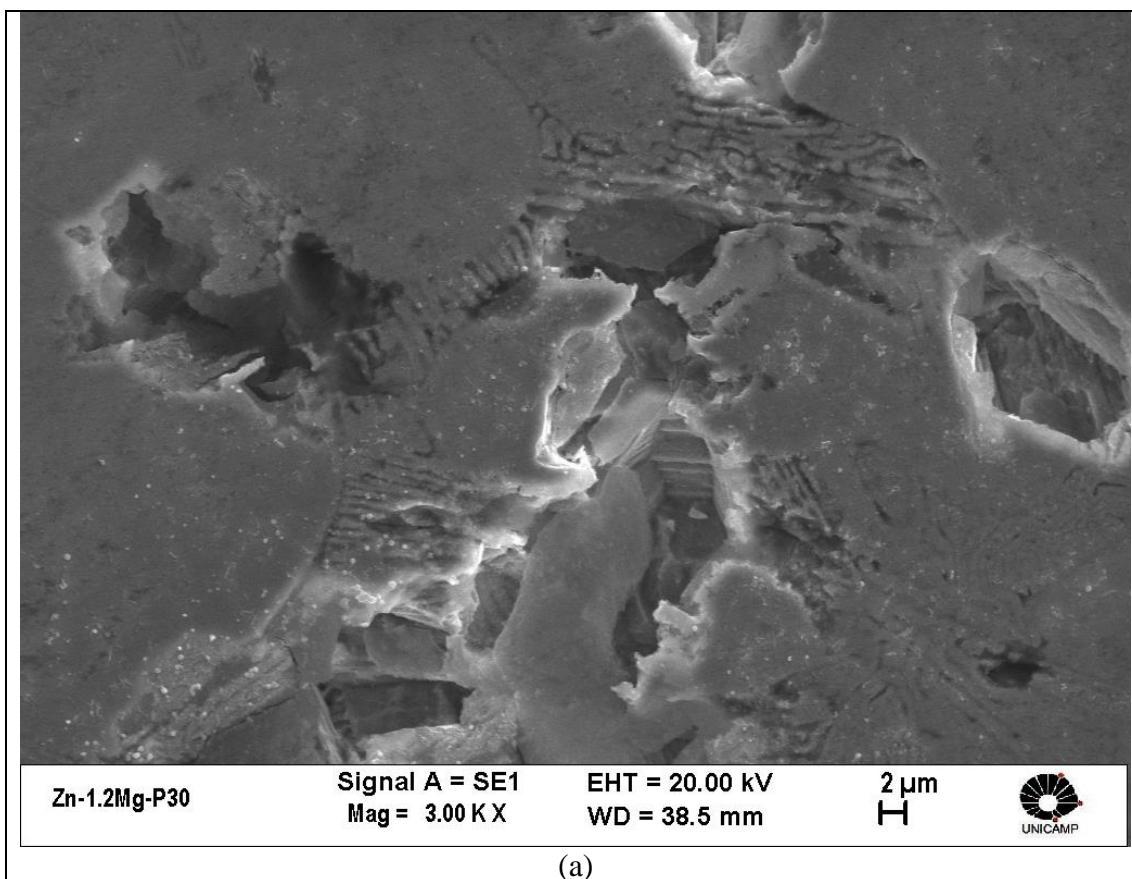
**Figure 7.** (a) and (b) Binary images (using the ImageJ<sup>®</sup> software) for the Zn-1.2 wt.% Mg and Zn- 2.0 wt.% Mg alloys, respectively; and (c) their corresponding Zn-rich area percentage (white region); and (d) and (e) magnifications of binary images showing the eutectic mixture of alloys samples examined and their corresponding Zn area percentages.

Besides, from the metallurgical point of view, when the alloy Mg content is increased, the eutectic fraction (ef) also increases, and consequently, Zn-rich areas (nobler areas) decrease correspondingly. In this sense, the micrographs shown in Figs. 1(a) to (d) were converted into binary images (using the ImageJ<sup>®</sup> software), where the black and white areas constitute active (eutectic mixture, Mg rich region) and nobler regions (Zn-rich dendritic matrix), respectively. Fig 7 shows both binary images and percentage of Zn-rich areas (nobler areas) evidencing that with the increase in the

Mg content, the resulting cathode-to-anode area ratios ( $A_c/A_a$ ) have been modified. When the binary images in Fig. 7(a) and (b) were analyzed, at least an area of  $\sim 420,000 (\pm 1,000) \mu\text{m}^2$  was considered. When Fig. 6(d) and (e) were analyzed an area of  $\sim 1,225 (\pm 100) \mu\text{m}^2$  was considered. The  $A_c/A_a$  ratio decreases of about 1.5 times when the alloy Mg content increases from 1.2 to 2.0 wt.%. This decrease in the  $A_c/A_a$  ratio has a deleterious effect on both the potentiodynamic and EIS parameters of the Zn-2.0 wt.% Mg alloy. Consequently, the corrosion action is more drastic and intense when compared with that occurring in the Zn-1.2 wt.% casting alloy sample.

Fig. 8(a) and (b) depict post mortem SEM images after EIS and potentiodynamic polarization tests in a 0.06 M NaCl solution at the environmental temperature for the Zn-1.2 and Zn-2.0 wt.% Mg alloys samples, respectively. Since Zn-rich regions are nobler with respect to the eutectic mixture and that inside the eutectic mixture both  $\text{Zn}_2\text{Mg}$  and  $\text{Zn}_{11}\text{Mg}_2$  IMCs are more active when compared with the Zn-rich dendritic matrix, preserved Zn-rich areas and selective corrosion of the Mg-rich lamellae were expected to occur.

It is worth noting that the eutectic areas are preferentially corroded in the microstructure network. Although it is not possible to determine which IMC is firstly corroded, these post mortem images indicate that both IMCs have deteriorated. It seems that eutectic array detaches from the lattice and pitting occurs.



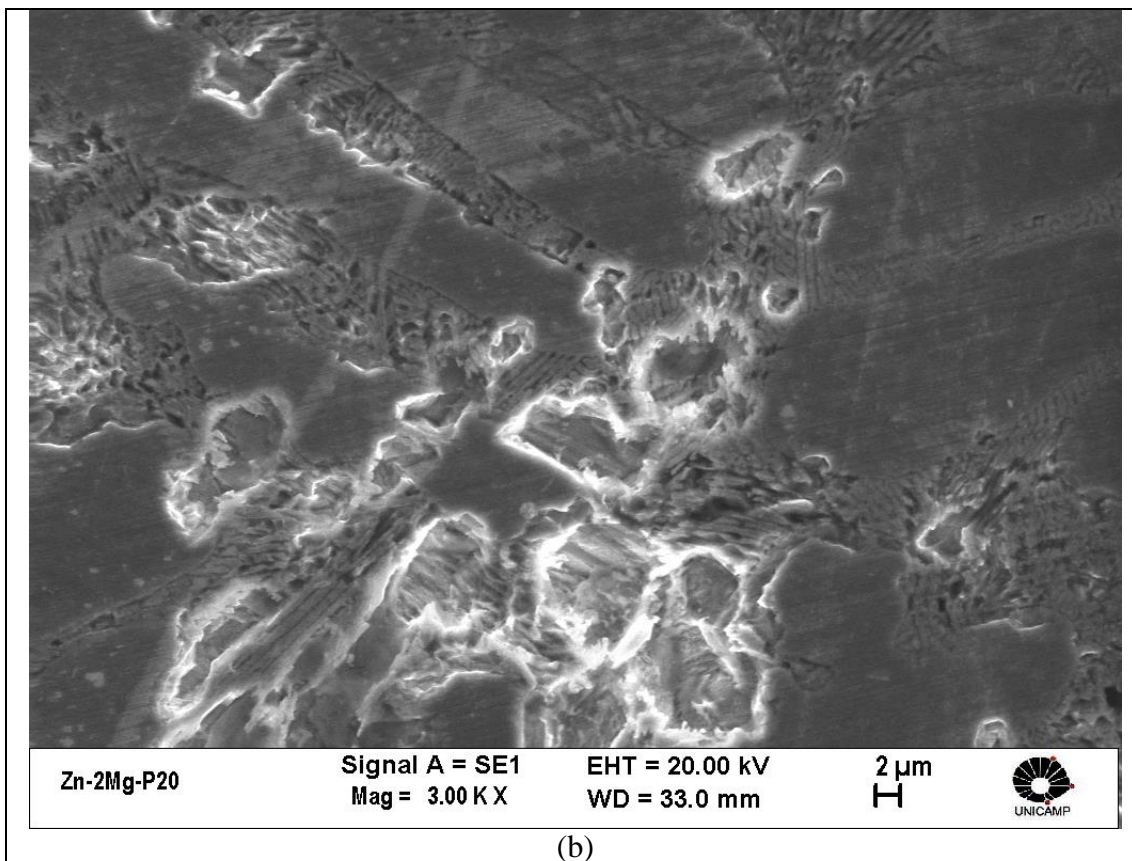


**Figure 8.** Typical post-mortem SEM images of the: (a) Zn- 1.2 wt.% Mg alloy and (b) Zn- 2.0 wt.% Mg alloy after EIS and potentiodynamic polarization measurements.

Since biomedical applications demand biodegradable and bioabsorbable materials, it seems that both Zn-1.2 and 2.0 wt.% alloys examined have potential to be used. However, depending of the type of implant (size and functionality) and local of the implantation (bone structure replacement or stent application), which implies mechanical integrity up to their total biodegradation/dissolution preventing irritation or inflammation reactions, additional investigations including *in vitro* (SBF solution) and *in vivo* studies should systematically be developed. As a contribution from corrosionists and metallurgists, this investigation provides both electrochemical and metallurgical parameters that will be helpful in the preprogramming of operational solidification thermal parameters (e.g. alloy composition and cooling rate) with a view to providing appropriate microstructures and final application properties minimizing the associated costs.

#### 4. CONCLUSIONS

Considering the microstructural and EIS parameters, associated with corrosion potentials and corrosion current densities experimentally determined for both Zn-1.2 wt.% and 2.0 wt.% Mg casting alloys samples examined, the following conclusions can be drawn:

The increase in the alloy Mg content from 1.2wt.% to 2.0wt.% has induced a microstructural refinement (in both the Zn-rich matrix and the eutectic mixture) and consequently, the corrosion potential has been displaced toward the more active side, thus provoking a deleterious effect on the corrosion behavior of the Zn-2.0 wt.% Mg alloy. Besides, the corrosion current density increased, as a function of the decrease in the Ac/Aa (cathode-to-anode areas ratio) and consequently the Zn-1.2 wt.% Mg alloy was shown to have a comparatively higher corrosion resistance.

The analyses carried out with the potentiodynamic polarization curves (experimental EIS parameters) have corroborated the previous conclusion. The capacitances CPEs, mainly that correlated with the inner oxide film, *i.e.*  $CPE_{(2)}$ , associated with the polarization resistances  $R_2$ , have indicated that the increase in the alloy Mg content (from 1.2wt.% to 2.0wt.%) “activated” the corrosion susceptibility. Besides, the increase in Mg content has also induced partial or effective break of the passive oxide film firstly formed. The EIS parameters have also indicated susceptibility to pitting corrosion when inductance and correlated resistances were analyzed, confirming the trend indicated in the potentiodynamic polarization curves.

#### ACKNOWLEDGEMENTS

The authors acknowledge the financial support provided by FAEPEX-UNICAMP, CNPq - The Brazilian Research Council, FAPESP- São Paulo Research Foundation (grants 2013/23396-7 and 2014/50502-5), CNPEM and LNNano for the use of the X-Ray Diffraction (XRD) equipment.

#### References

1. C. Z. Yao, Z. C. Wang, S. L. Tay, T. P. Zhu and W. Gao, *J. Alloys Compd.*, 602 (2014) 101.
2. M. M. Alves, T. Prosek, C. F. Santos and M. F. Montemor, *Mater. Sci. Eng. C*, 70 (2017) 112.
3. P. K. Bowen, J. Drelich and J. Goldman, *Adv. Mater.*, 25 (2013) 2577.
4. N. W. Solomons, *Ann. Nutr. Metab.*, 62 (2013) 8.
5. G. Song, *Corros. Sci.*, 49 (2007) 1696.
6. B. R. Zeng, W. Dietzel, F. Witte, N. Hort and C. Blawert, *Adv. Eng. Mater.*, 10 (2008) B3.
7. H. Wang, Z. M. Shi and K. Yang, *Adv. Mater. Res.*, 32 (2008) 207.
8. Z. J. Li, X. N. Gu, S. Q. Lou and Y. Zheng, *Biomaterials*, 29 (2008) 1329.
9. Y. Song, S. Zhang, J. Li, C. Zhao, X. Zhang, *Acta Biomater.*, 6 (2010) 1736.
10. M. Jamesh, S. Kumar and T. S. N. S. Narayanan, *Corros. Sci.*, 53 (2011) 645.
11. S. X. Zhang, X. N. Zhang, C. L. Zhao, J. A. Li, Y. Song, C. Y. Xie, H. R. Tao, Y. Zhang, Y. H. He, Y. Jiang and Y. J. Bian, *Acta Biomater.*, 6 (2010) 626.
12. M. P. Staiger, A. M. Pietak, J. Huadmai and G. Dias, *Biomaterials*, 27 (2006) 1728.
13. P. Erne, M. Schier and T. J. Resink, *Cardiovasc. Intervent. Radiol.*, 29 (2006) 11.
14. P. Zartner, M. Buettner, H. Singer and M. Sigler, *Cardiovasc. Interv.*, 69 (2007) 443.
15. B. A. Shaw, E. Sikora and S. Virtanen, *Electrochem. Soc. Interface*, Summer (2008) 45.
16. P. R. Goulart, J. E. Spinelli, N. Cheung and A. Garcia, *Mater. Chem. Phys.*, 119 (2010) 272.
17. M. A. Pinto, N. Cheung, M. C. F. Ierardi and A. Garcia, *Mater. Character.*, 50 (2003) 249.
18. M. Durman, *Z. Metall.*, 89 (1998) 417.
19. L. R. Garcia, W. R. Osório, L. C. Peixoto and A. Garcia, *J. Electron. Mater.*, 38 (2009) 2405.
20. N. C. Verissimo, C. Brito, W. L. R. Santos, N. Cheung, J. E. Spinelli and A. Garcia, *J. Alloys Compd.*, 662 (2016) 1.
21. S. H. Cai, T. Lei, N. F. Li and F. F. Feng, *Mater. Sci. Eng. C*, 32 (2012) 2570.

22. S. H. Wei, T. P. Zhu, M. Hodgson and W. Gao, *Mater. Sci. Eng. A*, 550 (2012) 199.
23. F. X. Qin, G. Q. Xie, Z. Dan, S. L. Zhu and I. Seki, *Intermetallics*, 42 (2013) 9.
24. X. Liu, J. Sun, Y. Yang, Z. Pu and Y. Zheng, *Mater. Lett.*, 161 (2015) 53.
25. H. Y. Liu and H. Jones, *Acta Metall. Mater.*, 40 (1992) 229.
26. H. Y. Liu and H. Jones, *J. Mater. Sci. Lett.*, 11 (1992) 769.
27. T. A. Vida, E. S. Freitas, C. Brito, N. Cheung, M. A. Arenas, A. Conde, J. D. Damborenea and A. Garcia, *Metall. Mater. Trans. A*, 47 (2016) 3052.
28. B. Hirschorn, M. E. Orazem, B. Tribollet, V. Vivier, Isabelle Frateur and M. Musiani, *Electrochim. Acta*, 55 (2010) 6218.
29. B. Hirschorn, M. E. Orazem, B. Tribollet, V. Vivier, I. Frateur and M. Musiani, *J. Electrochem. Soc.*, 157 (2010) C458.
30. B. Hirschorn, M. E. Orazem, B. Tribollet, V. Vivier, I. Frateur and M. Musiani, *J. Electrochem. Soc.*, 157 (2010) C452.
31. P. C. Banerjee, R. K. S. Raman, Y. Durandet and G. McAdam, *Corros. Sci.*, 53 (2011) 1505.
32. Q. L. Yang, J. Xu, L. Chen, Y. L. Gong, X. Sun and C. G. Chen, *J. Electrochem. Soc.*, 164 (2017) A630.
33. J. Zhang, C. S. Dai, Z. H. Wen and J. Wei, *Int. J. Electrochem. Sci.*, 10 (2015) 6002.
34. N. Mahato and M. M. Singh, *Portugaliae Electrochim. Acta*, 29 (2011) 233.
35. W. R. Osório, N. Cheung, L. C. Peixoto, A. Garcia, *Int. J. Electrochem. Sci.*, 4 (2009) 820.
36. M. Zhao, S. Wu, P. An and J. Luo, *Appl. Surf. Sci.*, 253 (2006) 468.
37. G. M. Pinto, J. Nayak and A. N. Shetty, *Int. J. Electrochem. Sci.*, 4 (2009) 1452.
38. S. E. Frers, M. M. Stefenel, C. Mayer and Chierchie, *J. Appl. Electrochem.*, 20 (1990) 996.
39. M. A. Jinling, W. Jiuba, L. I. Gengxin and X. V. Chunhua, *Corros. Sci.*, 52 (2010) 534.
40. F. Mansfeld, *Electrochim. Acta*, 38 (1993) 1891.
41. R. G. Buchheit, *J. Electrochem. Soc.*, 142 (1995) 3994.
42. N. Birbilis and R. G. Buchheit, *J. Electrochem. Soc.*, 152 (2005) B140.
43. W. R. Osório, L. C. Peixoto, P. R. Goulart and A. Garcia, *Corros. Sci.*, 52 (2010) 2979.
44. D. S. Gandel, M. A. Easton, M. A. Gibson and N. Birbilis, *Corrosion*, 69 (2013) 666.
45. Z. P. Cano, J. R. McDermid and J. R. Kish, *J. Electrochem. Soc.*, 162 (2015) C732.
46. R. Walter, M. B. Kannan, Y. He and A. Sandham, *Mater. Lett.*, 130 (2014) 184.
47. P. Vanýsek, *Electrochemical Series*, In: Haynes, W. M. *Handbook of Chemistry and Physics: 93rd Edition*. Chemical Rubber Company. (2012) 5. ISBN 9781439880494.
48. R. Krieg, A. Vimalanandan and M. Rohwerder, *J. Electrochem. Soc.*, 161 (2014) C156.